Electronic Supplementary Information for

Flexible bifunctional sensor based on porous copper nanowires@IonGels composite films towards high-resolution stress/deformation detection

Shaohui Zhang[a,b], Chao Wang[a,b], Liuyi Ding[a,b], Long Zhang[a,b], Jiafan Chen[b], Hui Huang[a,b], Dapeng Jiang[b,c], Ziyang Chen[b] and Gebo Pan*[a,b]

a School of Nano-Tech and Nano-Bionics, University of Science and Technology of China, No. 96, Jinzhai Road, Baohe District, Hefei, 230026, P. R. China
b Division of Interdisciplinary and Comprehensive Research & Platform for Characterization and Test, Suzhou Institute of Nano-Tech and Nano-Bionics, Chinese Academy of Sciences, No. 398, Ruoshui Road, Industrial Park, Suzhou, 215123, P. R. China
c Nano Science and Technology Institute, University of Science and Technology of China, No. 166, Ren'ai Road, Industrial Park, Suzhou, 215123, P. R. China

_____

*Corresponding author at:

Suzhou Institute of Nano-Tech and Nano-Bionics, Chinese Academy of Sciences, 215123 Suzhou, P. R. China.

Telephone: +86-0512-62872663. E-mail: gbpan2008@sinano.ac.cn (G.-B. Pan)
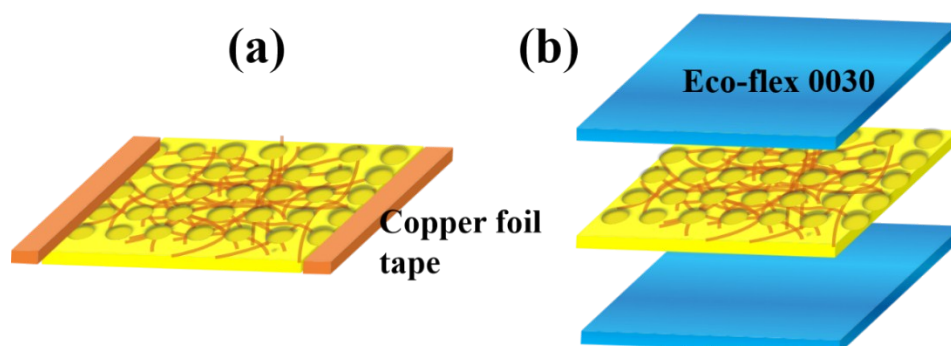

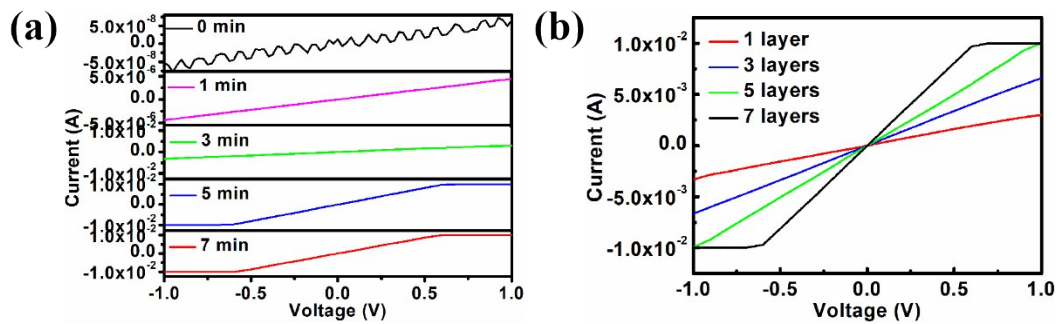Fig. S1 Constructed (a) strain and (b) pressure sensor schematic diagram

Fig. S2 Optimization of (a) optimum cleaning time and (b) number of spray coatings
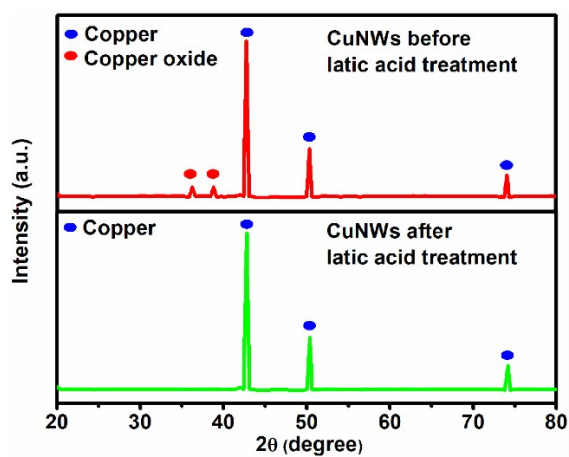

Fig. S3 The XRD comparison of CuNWs solution before and after lactic acid washing
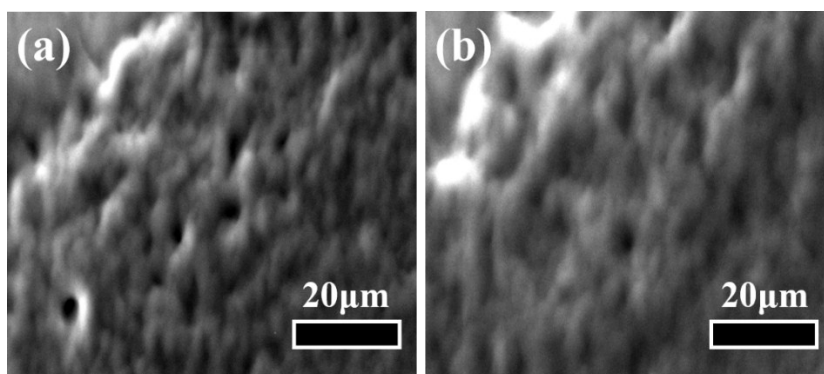

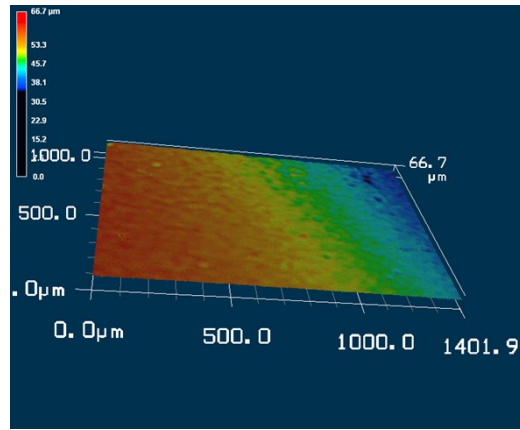Fig. S4 The SEM image of PCIs after washing with NMP and absolute ethanol
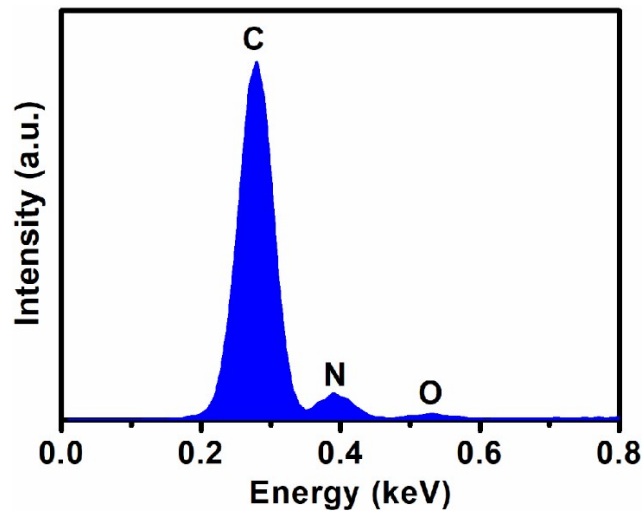
Fig. S5 CLSM 2D imaging of the PCIs sample

Fig. S6 The EDS spectrum of IonGels

Element	Wt%	At%
CK	47.29	51.44
NK	51.86	48.38
CuK	00.85	00.18
Matrix	Correction	ZAF

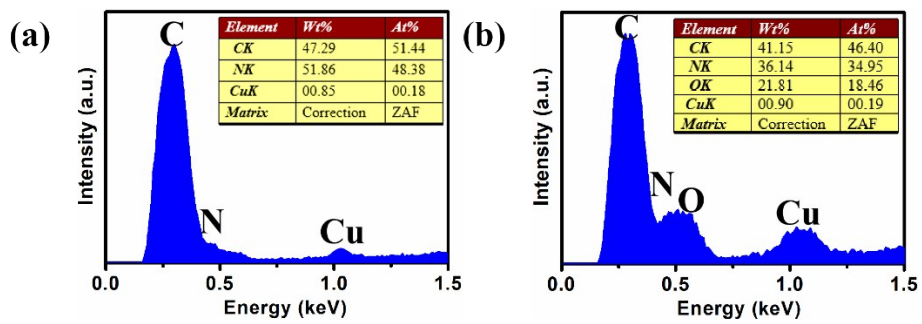| Element	Wt%	At%
CK	41.15	46.40
NK	36.14	34.95
OK	21.81	18.46
CuK	00.90	00.19
Matrix	Correction	ZAF

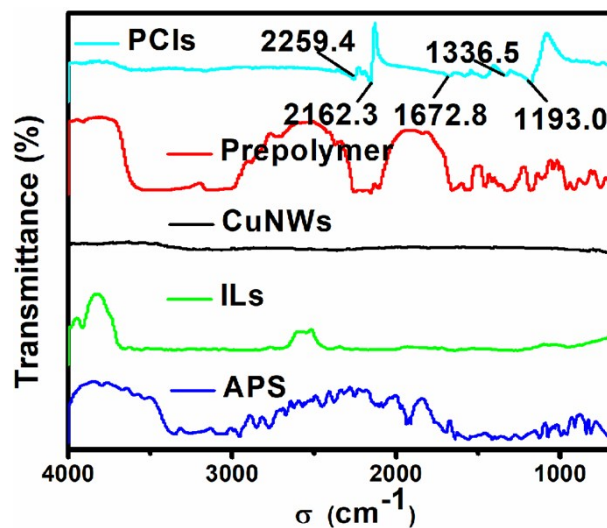Fig. 7 The EDS contrast spectra of PCIs before (a) and after (b) washing

Fig. S8 FT-IR spectrum comparison of all reactants and prepolymers involved in IonGels synthesis
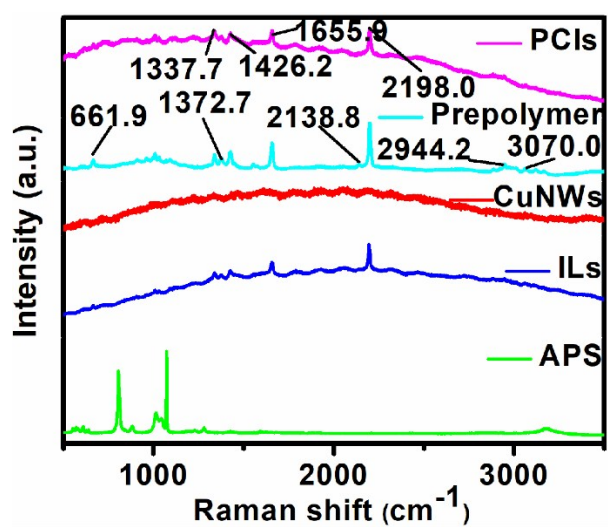

Fig. S9 Raman spectrum comparison of all reactants and prepolymers involved in IonGels synthesis

The mechanism of the IonGels synthesized in this work was analyzed in depth (Fig. S10). In addition to the ionic conductivity of the ionic liquid itself, the entire process also included the synergistic effect of strong (formed between ionic liquid and exchange solvent) and weak (formed between anion and cation of ionic liquid) hydrogen bonds, the conductive nanochannels formed after self-polymerization and dynamic cross-linking together endowed the IonGels super mechanical properties, dynamic stability, and good recoverability.
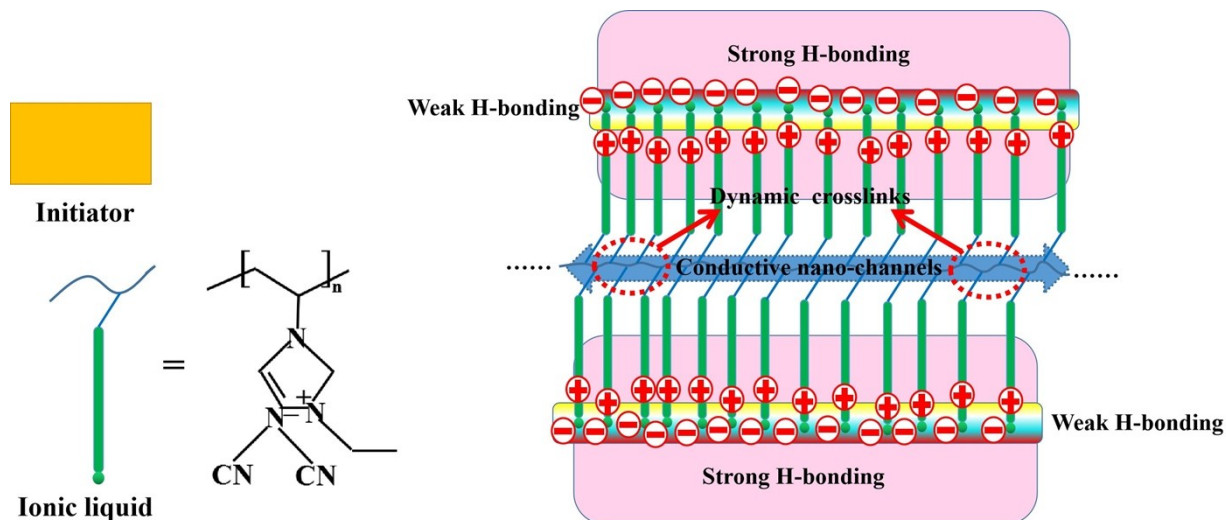

Fig. S10 Schematic diagram of the preparation mechanism of self-polymerizing IonGels

Specifically, Figure S11 showed the stress‑strain curves of IonGels during the loading‑unloading process at different strains. Hysteresis phenomena were observed, which indicated that IonGels had the ability to dissipate energy. Theoretically, the energy dissipation ability of IonGels might originate from the disentanglement of polymer chains, breakage of possible hydrogen bonds, and rupture of chemical cross-linking points. Hysteresis loops were observed and the dissipated energy produced a slight decrease with the increasing cycling number. This meant that the inter- or intra-chain interactions were gradually broken during mechanical deformation and dissipate energy. The excellent toughness and fatigue resistance of the IonGels provided an opportunity to fabricate highly durable flexible sensors.

The IonGels were conductive due to the existence of large amount of ions as charge carriers in their networks. The ionic conductivity of IonGels was comparable to that of pure ILs [VEIm][DCA]. This meant that the mechanical deformation was converted to detectable electrical current, electrical durability without any degradation even after the extreme stretching.
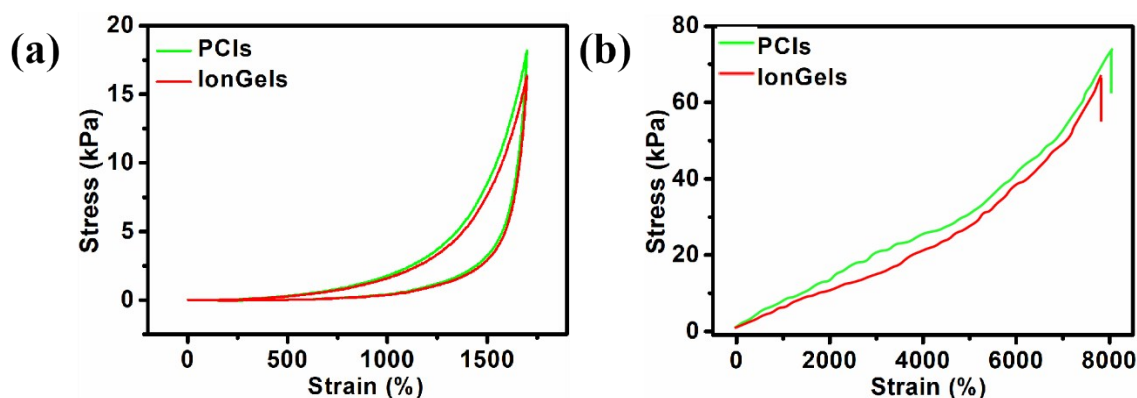

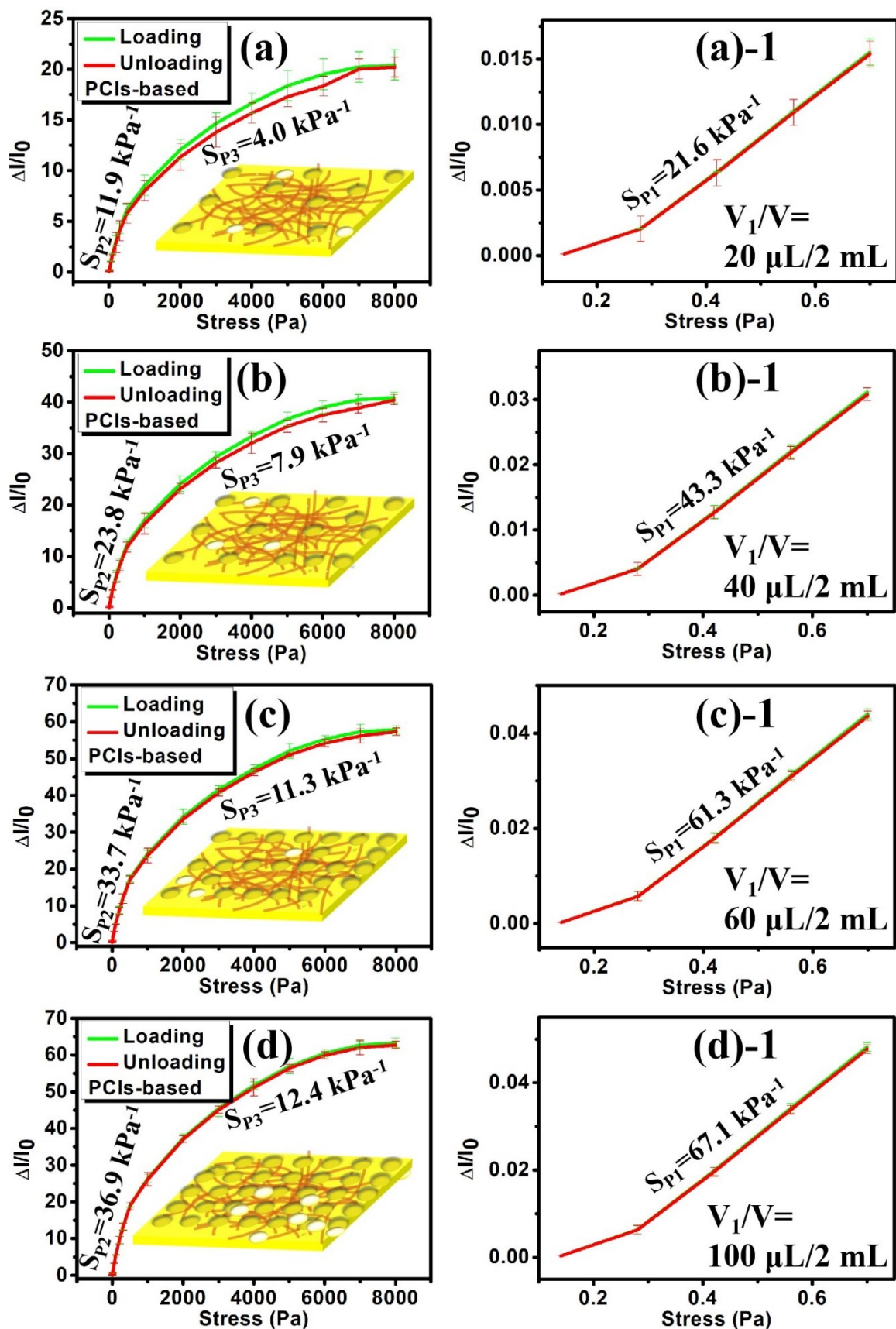Fig. S11 The curve of elastic modulus versus strain measured by Mark-10

Fig. S12 The relative current vs. pressure curves (a-d) and partial magnification curves ((a)-1 to (d)-1) of stress sensors based on PS microspheres with different doping volume fractions. (a) V1/V=20 μL/2 mL. (b) V1/V=40 μL/2 mL. (c) V1/V=60 μL/2 mL. (d) V1/V=100 μL/2 mL
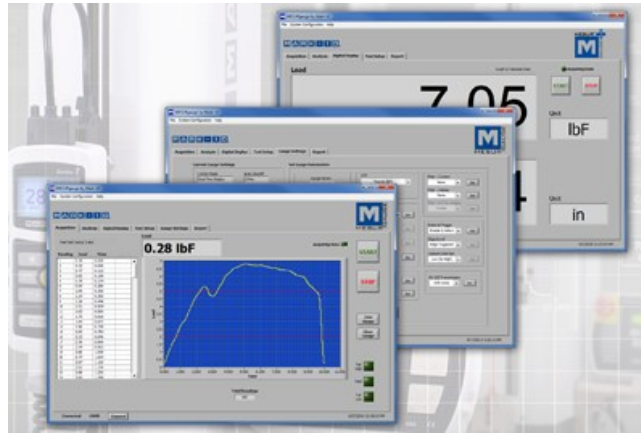
Fig. S13 Data collection & motion control software-USB output of force vs travel

Fig. S14 The tester mimicked the trembling photo of Parkinson's patients

The Fig. S15 were the enlarged profiles of one cycle in Fig. 7f. The comparison of the pressure pulse waves showed apparent differences under different stress. To further quantify the difference between the pulse waves, two of the most commonly used parameters are defined: the augmentation index (**AIx**):

$$\text{AIx (\%)} = \pm(P_S - P_i)/PP = \pm \Delta P/PP$$

and the reflection index (**RI**):

$$\text{RI} = h/\Delta t$$

where h is the subject height, Δt is the time delay between P_S and P_D, while PP is the absolute pulse wave magnitude. As shown in Fig. 7f, based on the continuous arterial pulse waves, a statistical result of the AIx and RI was recorded for the young man, corresponding values of -20.8% and 8.4 m/s were recorded for the parameters AIx and RI. As summarized in Fig. S15, all the typical characteristics of wrist pulses obtained by the above sensor clearly contains P_S, P_i, P_T, valley, and P_D, suggesting the potential application of this sensor in clinical medicine for pulse measurement.
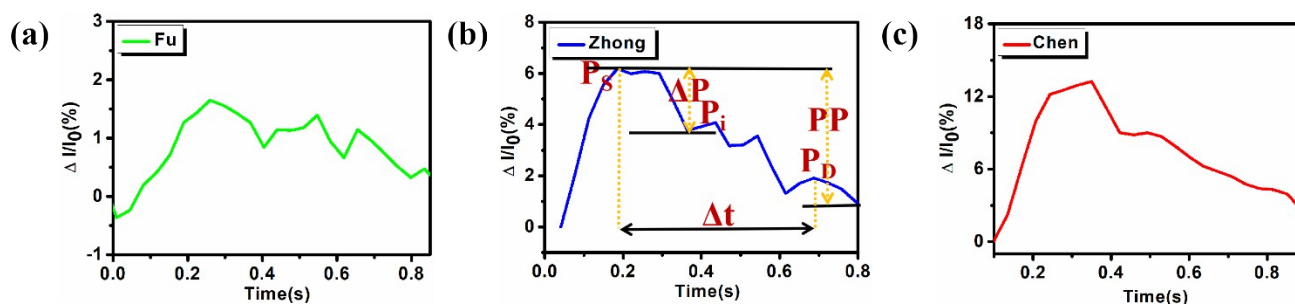

Fig. S15 Tester's three different types enlargement images of pulse-wave. (a)Fu. (b) Zhong. (c) Chen

References:

S1 C. Luo, N. Liu, H. Zhang, W. Liu, Y. Yue, S. Wang, J. Rao, C. Yang, J. Su, X. Jiang and Y. Gao, *Nano Energy*, 2017, **41**, 527-534.

S2 C. Garcia, I. Trendafilova, R. G. de Villoria and J. S. del Rio, *Nano Energy*, 2018, **50**, 401-409.

S3 C. Hou, Z. Xu, W. Qiu, R. Wu, Y. Wang, Q. Xu, X. Y. Liu and W. Guo, *Small*, 2019, **15**, 1805084.

S4 W. Fu, Y. Dai, X. Meng, W. Xu, J. Zhou, Z. Liu, W. Lu, S. Wang, C. Huang and Y. Sun, *Nanotechnology*, 2018, **30**, 045602.

S5 T. G. Yun, M. Park, D. H. Kim, D. Kim, J. Y. Cheong, J. G. Bae, S. M. Han and I. D. Kim, *ACS Nano*, 2019, **13**, 3141-3150.